

Design and Analysis of a Bi-Directional Ducted Tidal Turbine

Conor F. Fleming*, Simon C. McIntosh and Richard H.J. Willden

Department of Engineering Science, University of Oxford

Parks Road, Oxford, OX1 3PJ, UK

E-mail: *conor.fleming@eng.ox.ac.uk

Abstract—A duct for a tidal turbine is designed through simulation and analysis of a series of candidate geometries in which internal and external curvature are varied. Duct performance is evaluated in terms of power extraction and basin-scale efficiency, where the rotor is modelled as an actuator disk. The effects of surface curvature are identified: a flat external surface limits the size of the separated recirculating flow downstream of the leading edge of the duct thereby reducing losses, and increased curvature of the duct inner surface leads to increased flow velocity, but at the expense of rotor area. A degree of internal curvature is found which achieves the best balance between flow acceleration and power-extracting area. The best bi-directional ducted device only achieves a maximum power of 57% of the equivalent diameter unducted device.

Two sets of subsequent simulations, including modelling of the rotor itself, are carried out for a selected duct design. In the first set, the axial and tangential forces on the rotor are calculated using blade element momentum theory and applied at the rotor plane. In a second series of blade-resolved simulations, the rotor geometry is explicitly captured by the mesh. Angular motion of the rotor is achieved through a sliding mesh technique. The two methods of rotor modelling are then compared in terms of power extraction and basin efficiency. The tip-losses usually associated with rotor flows, attributable to vortex shedding from the blade tips, are limited by the duct.

Index Terms—tidal, turbine, duct

I. INTRODUCTION

Many tidal energy converters currently in development feature a ducted rotor [1], [2]. Significant performance improvements for ducted devices over unducted devices have been reported both by developers and researchers [3], [4]. In this work, the mechanisms by which the duct increases velocity at the rotor plane are investigated. A series of candidate duct designs (denoted A to H), with wide variations in surface curvature are produced and simulated using the Reynolds Averaged Navier Stokes (RANS) solver ANSYS FLUENT [5]. For comparative purposes, an unducted device is also modelled. For simplicity, rotors are represented using actuator disks, that mimic lossless energy extraction. Duct parameters that lead to desirable performance characteristics are identified and incorporated into a more optimal design.

Two further methods of rotor modelling, expected to produce more realistic performance characteristics, are described and compared to the ideal actuator disk result.

II. DESIGN CONSIDERATIONS

Conventionally, in comparisons between ducted and unducted devices, the rotor diameter is held constant. Consequently, it is unclear whether any resulting improvement in performance is due to acceleration of the flow by the duct, increased flow blockage or increased upstream capture width. The available power, P , within a streamtube is

$$P = \frac{1}{2} \rho A u_{\infty}^3 \quad (1)$$

where ρ is the fluid density, A is the cross-sectional area of the streamtube, and u_{∞} is the free-stream flow speed. The motivation for enclosing a rotor within a duct is to increase the flow velocity at the rotor, leading to an increase in available power.

To facilitate comparison between competing duct designs we choose to hold external blockage constant by using a constant maximum outer dimension for each duct, while the rotor diameter is allowed to vary within the duct according to its internal surface curvature. A duct length-to-diameter ratio of 1 : 1 is used throughout, an aspect ratio that reflects observations of current commercial designs [1]. A ducted device of the same external dimension is simulated for comparative purposes. Schematic diagrams of the test series are laid out in Fig. 1.

Geometries A to G are produced by systematically varying the curvature of the internal and external duct surfaces. Duct H is designed based on the performance results of the preceding designs, and features the internal surface of Duct D and the external surface of duct B.

III. SOLUTION METHOD

A. Domain Dimensions

The dimensions of the computational domain are based on an experimental flume in which future comparative experiments will be carried out. This flume is 1.5 m wide and can accommodate flows of up to 1 m in depth. A duct diameter, D , of 0.4 m is chosen to achieve relative dimensions representative of a full-scale installation. There is also a desire not to overly block the flow or overly constrain external flow features (separations) that have been observed in previous studies of ducted turbines [6]. This results in horizontal blockage of 27% (equivalent to an inter-device spacing of 3.75 as the vertical walls are modelled as symmetry planes), vertical blockage of

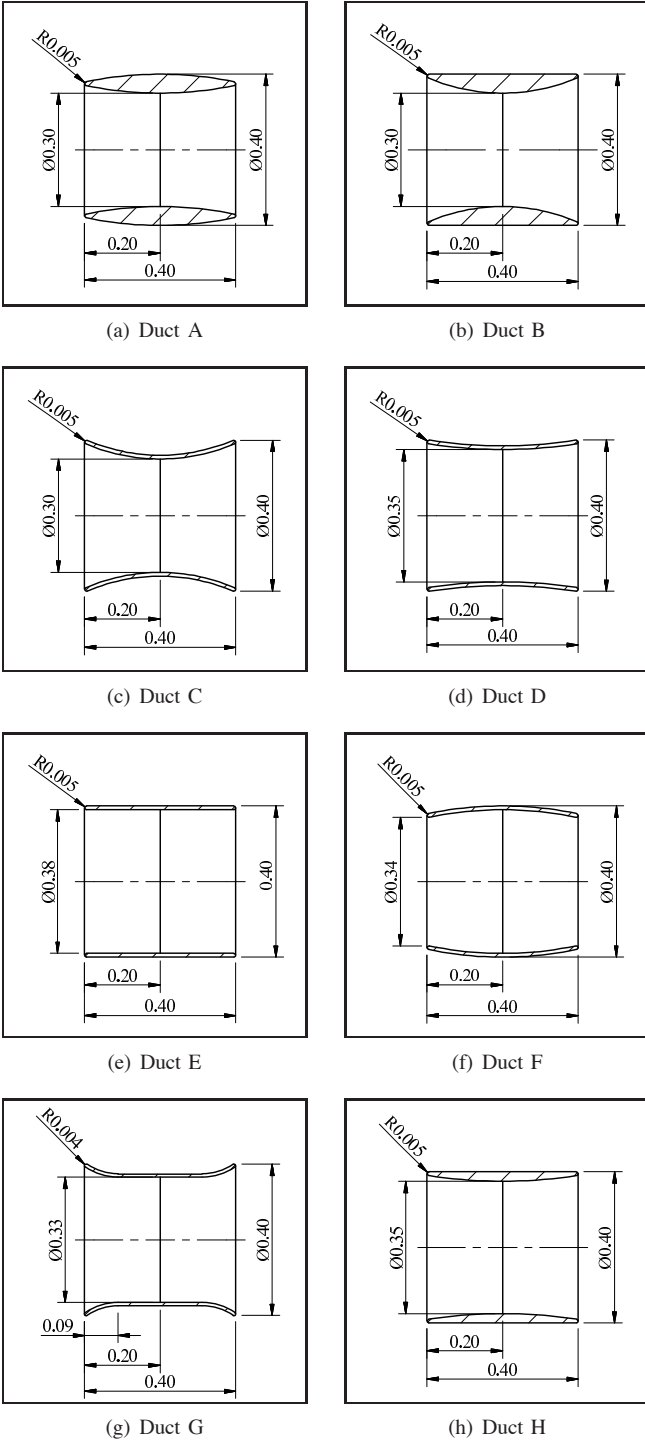


Fig. 1. Schematic diagrams of candidate duct designs. Duct H combines features of ducts B and D. All dimensions are in metres.

40%, and area blockage of $b \approx 8\%$. The unducted device also has a diameter of 0.4 m.

A requirement of a broad parametric study such as this is that solution time be minimised. Hence reductions in overall cell count are sought.

The inlet boundary is set three diameters upstream of the rotor plane. Flow uniformity upstream of the turbine, together

with the bound nature of tidal flows, permits this choice of boundary placement.

The same assumptions do not hold for the downstream boundary, where sheared, highly turbulent flow may be encountered. To determine the effect of outlet distance, four computational domains are trialled, with downstream domain lengths of three, six, twelve and twenty-four diameters respectively. For all boundary distances trialled, static pressure is found to be invariant at a common plane three diameters downstream of the rotor. Accordingly, a vanishingly small change in rotor performance due to downstream placement is observed. A downstream domain length of three diameters is hence deemed to be satisfactory and is used for all subsequent simulations.

B. Mesh Generation

Mesheres are generated using a highly automated method, where target cell dimensions are specified at boundaries, surfaces and density regions, and the domain is filled with unstructured tetrahedral elements according to the Octree algorithm [7]. Some degree of control over the local mesh is relinquished in favour of robust and efficient mesh generation. While coordinates of cell nodes and centroids will not individually correspond between meshes, the general topology remains consistent.

In order to fully resolve the boundary layer on the duct surface, the tetrahedral elements adjacent to the surface are replaced with layers of high-aspect ratio prismatic elements. The wall-adjacent cell height is set to achieve a non-dimensional wall distance of $y^+ = 1$, where $y^+ = (y/\nu)(\tau_w/\rho)^{\frac{1}{2}}$ and y , ν , and τ_w are the wall normal distance, kinematic viscosity, and wall shear stress respectively.

Appropriate mesh resolution is determined based on a grid convergence study on duct D, where a uniform global scaling factor is adjusted. This scaling factor modifies the target cell dimension settings prior to mesh generation. For a scaling factor less than unity, the resulting mesh consists of smaller elements, and vice versa. The wall-adjacent cell height, and hence y^+ , are not affected. The influence of mesh resolution on the distribution of the pressure coefficient, c_p , around a section of duct D is highlighted in Fig. 2. The pressure jump is identifiable as the dramatic change of slope in the upper portion of the curve. The slope of this line is a consequence of the distance between cell centroids across the face of the porous disk, and only the magnitude of the pressure drop is of concern. Differences between the three meshes are discernible on the suction surface. The lowest resolution mesh predicts reattachment of flow noticeably earlier than the other meshes. This result, and similar results for wake velocity profiles, show that the base mesh (scaling factor of 1.0) is over-resolved, so the medium-resolution mesh (scaling factor of 1.5) is adopted for the duct performance comparisons.

The meshes used for the duct comparison simulations typically contain around one million elements.

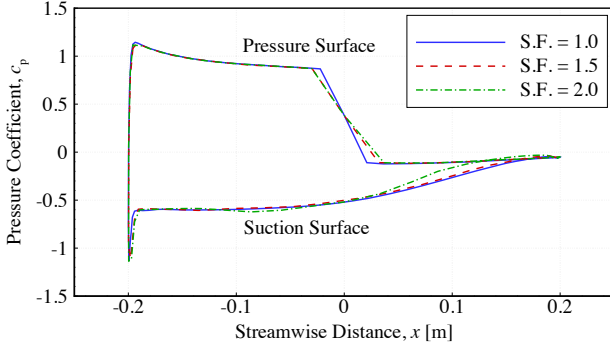


Fig. 2. Distribution of power coefficient, c_p , around a section of duct D for three levels of mesh resolution, as defined by global scaling factors of 1.0 (high resolution), 1.5 (medium resolution), and 2.0 (low resolution).

C. Computational Setup

Closure of the RANS equations is achieved through the use of the $k-\omega$ SST turbulence model, which is capable of modelling flow separations, as can occur in ducted flows. In the absence of turbulence-generating mechanisms, such as sheared inflow and wall roughness, inflow turbulence intensity levels representative of the tidal environment ($\sim 10\%$) are not sustainable, and decay by an order of magnitude between the inlet and rotor plane. Effective modelling of the highly-turbulent tidal environment is likely to require the specification of unsteady and sheared inflow profiles and will be investigated in future work. For these comparative simulations, effects of turbulence are minimised by setting a low level of turbulence intensity (0.1%). The turbulent length scale is set to 0.2 m, based on device radius. For such a low level of turbulence intensity, the length scale parameter in the $k-\omega$ SST model will have a negligible effect on device performance.

Experimental testing will be carried out at a Froude number representative of real tidal flows. By setting an inflow velocity of 0.27 m s^{-1} and a water depth of 1.0 m, a Froude number of $Fr = 0.086$ is achieved. For the simulations presented here, the same velocity of 0.27 m s^{-1} is specified at the inlet to match the experimental setup.

A constant static pressure of 0 Pa is set across the outlet. The floor and sidewalls are modelled using symmetry conditions. The free surface is modelled as a rigid lid (symmetry) rather than as a deformable free surface, which is deemed sufficient for the low blockage conditions under consideration [8].

The focus of this initial series of simulations is on capturing the hydrodynamics of the duct effectively. Local flow features pertaining to the rotor, such as swirl and variable blade loading, are of lesser significance at this stage. The axial thrust of the rotor is important and must be modelled. Computational load is also a primary concern, as many candidate duct geometries must be simulated for a full range of operating points. These requirements can be met by modelling the rotor as a porous disk, a method that has been validated against one-dimensional momentum theory by Belloni and Willden

[9].

The porous disk acts to impose a pressure jump, Δp , across the disk that mimics the thrust on a real rotor. The pressure jump is dependent on the local velocity normal to the disk, u_d , and a porous loss factor K_L as defined in equation 2. The full range of disk operating points is found to be achieved by varying K_L from 0 to 4.

$$\Delta p = K_L \frac{1}{2} \rho u_d^2 \quad (2)$$

Unsteady simulations are carried out on the series of disk embedded ducts in order to capture time-dependent flow features such as vortex shedding. A timestep size of 0.01 s is chosen, and simulations are run for 12 s of flow time, with lift and drag forces on the duct converging in 8 – 10 s.

Subsequent steady simulations show however that the performance metrics of interest, power and thrust coefficients (C_P and C_T), are unaltered between steady and unsteady flows.

IV. PERFORMANCE METRICS

A. Induction Factor

The velocity at the rotor plane is described in terms of an induction factor

$$a = 1 - \left(\frac{\overline{u_d}}{u_\infty} \right) \quad (3)$$

where the overbar infers the average value over the disk plane.

B. Coefficients of thrust and power

The coefficients of thrust and power are defined in Eqs. 4 and 5,

$$C_T = \frac{T}{\frac{1}{2} \rho A_{\text{ref}} u_\infty^2} \quad (4)$$

$$C_P = \frac{P}{\frac{1}{2} \rho A_{\text{ref}} u_\infty^3} \quad (5)$$

where T is the axial thrust on the disk and A_{ref} is the cross-sectional area based on the external diameter of the duct. We choose this dimension for reference to provide a constant comparative basis between candidate designs. We also believe that this is the fairest mechanism by which devices should be compared as it expresses power generated to that available in the unperturbed streamtube intersected by the whole device; the rotor together with its required external duct. Further, it is likely that depth will dictate external device dimension at many sites so that it is this dimension and not rotor diameter *per se*, that would be held constant in a candidate design study for a real tidal site.

The extracted power, P , is calculated by equation 6.

$$P = \frac{1}{2} K_L \rho \overline{u_d^3} A_{\text{ref}} \quad (6)$$

The thrust force on the disk and duct is calculated in a similar manner.

$$T = \frac{1}{2} K_L \rho \overline{u_d^2} A_{\text{ref}} \quad (7)$$

These methods compare well with the control volume method for thrust and power evaluation employed by Belloni and Willden [6].

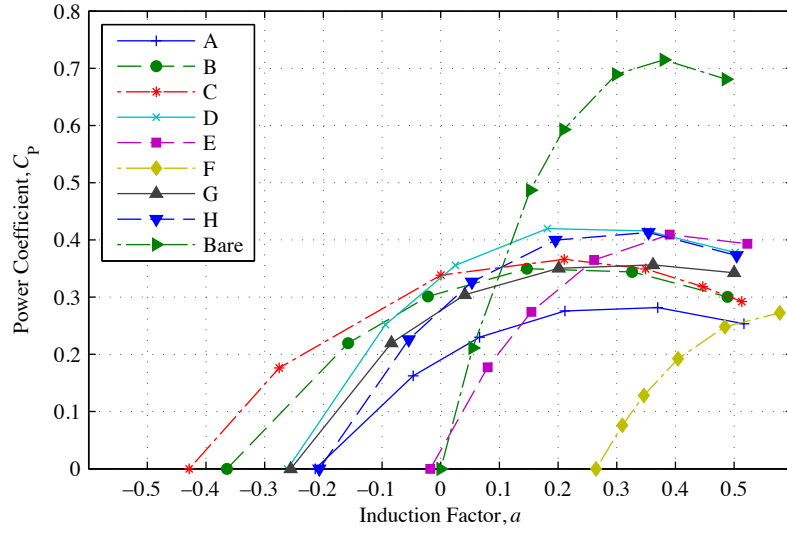


Fig. 3. Comparison of power coefficient for ducts A to H and the bare unducted disk.

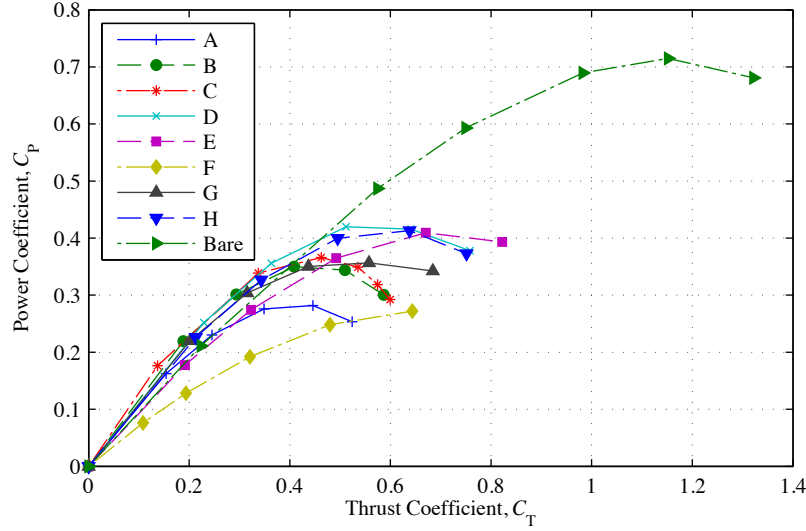


Fig. 4. Comparison of disk thrust coefficient for ducts A to H and the bare unducted disk.

C. Basin efficiency

The coefficient of power is a measure of disk power relative to the kinetic power available from the flow in the absence of the turbine. Power lost due to viscous effects and wake mixing is not accounted for by the C_P metric. From a thermodynamic standpoint, the mixing of two or more streams of dissimilar velocities, as occur in turbine wakes between core and bypass flows, will result in an increase in the mixed flows entropy and hence represents a departure from the reversible state. Such losses are accounted for through the definition of a basin efficiency, η , defined here as the ratio of disk power, P , to total power removed from the flow, being $P + P_{\text{losses}}$, where the latter term is the power lost; see equation 8. In order to conserve the finite tidal resource for other devices operating within the same tidal stream, a high basin efficiency is desirable. The definition used here differs slightly from that

of Shives and Crawford [10] as losses due to wake mixing beyond the computational domain are accounted for.

$$\eta = \frac{P}{P + P_{\text{losses}}} \quad (8)$$

The denominator in equation 8 is calculated by taking the difference between the energy fluxes through an unperturbed plane upstream of the turbine and a theoretical plane far downstream (station B - see Fig. 5), where the turbine wake and bypass flows have fully remixed to establish a uniform flow velocity. The denominator therefore represents the total power removed from the flow. Equation 8 can thus be re-expressed as follows:

$$\eta = \frac{P}{\int_{\text{inlet}} p_o u \, dA - \int_B p_o u \, dA} \quad (9)$$

where p_o is total pressure, u is the streamwise component of

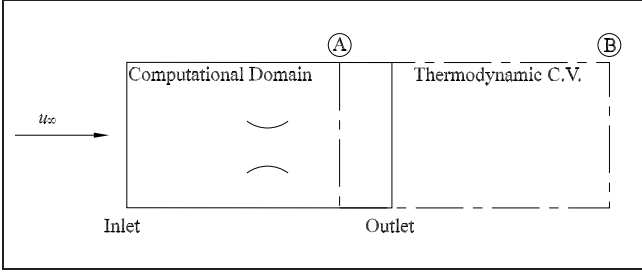


Fig. 5. Schematic representation of thermodynamic control volume for calculation of basin efficiency.

velocity, and the integration is taken over a plane normal to the freestream flow direction. The total pressure at station B can be calculated through equation 10, having first determined the static pressure, P , at station B through conservation of streamwise linear momentum (equation 11) over a control volume spanning stations A to B downstream of the turbine (see Fig. 5);

$$p_{o,B} = p_B + \frac{1}{2}\rho u_\infty^2 \quad (10)$$

$$\int_A p dA - \int_B p dA = \int_B \rho u^2 dA - \int_A \rho u^2 dA \quad (11)$$

where conditions at station B are such that p_B is uniform and the flow velocity recovers to the upstream flow velocity, u_∞ . Note that the free-surface is modelled as a rigid lid and therefore undergoes no change in height. The inlet of the control volume, station A, is set between the turbine and the outlet of the computational domain as far upstream as is possible in order to minimise unphysical numerical dissipation losses. The analysis presented above is readily extendable to the case of a deforming free surface in which gravitational potential changes together with free surface height changes must be considered.

V. DUCT EVALUATION

Comparisons of power and thrust coefficients for ducts A – H as well as the bare unducted device are plotted as functions of induction factor a in Figs. 3 and 4 respectively.

In both figures, the most prominent device is the unducted rotor. The best bi-directional design, device D, attains a maximum power coefficient C_P of only 57% of the maximum C_P for the unducted device. Note that as in the present case of blocked flow the power coefficient can exceed the theoretical maximum for unbounded flow; the Betz limit for which $C_P|_{\max} \approx 0.593$. For the present case of 8.4% blockage the upper limit on C_P can be computed from linear momentum theory to be 0.706 [11], which is close to the maximum observed for the unducted disk in Fig. 3.

One effect of a converging-diverging duct (A, B, C, D, G, and H) upon a rotor is to broaden the operating range of the rotor into the negative induction factor region, indicating an acceleration of disk flow velocities to magnitudes greater than freestream. The curved surface of the duct accelerates the internal flow beyond the freestream velocity. While an

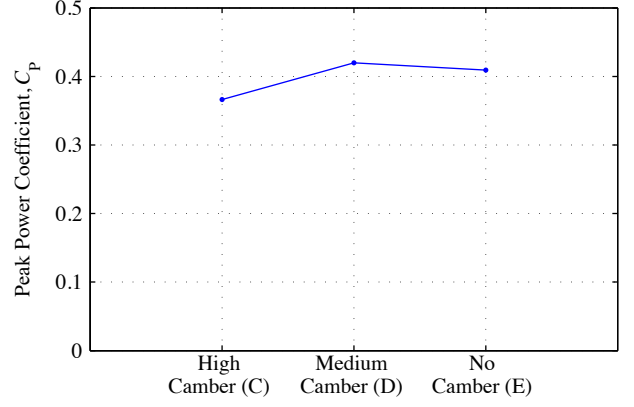


Fig. 6. Effect of duct camber on peak power coefficient.

increase in curvature leads to a desirable increase in disk velocity, it also necessitates an undesirable reduction in disk diameter. The trade-off between duct camber and disk area is highlighted in Fig. 6, where the peak power coefficients of ducts C (high camber), D (medium camber) and E (no camber) are compared. Duct D achieves the best balance between flow acceleration and power-extracting area, resulting in maximum C_P .

Ducted turbines generally have lower basin efficiencies than unducted devices due to the additional loss mechanisms associated with added streamwise loading, or drag, on the duct (see Fig. 10). Figure 7 shows how the flow recirculates within the cavity on the external surface of the inwardly curved ducts (such as duct C) after separating at the leading edge. Associated viscous and pressure losses [6], [9] may be reduced and hence basin efficiency improved by filling in this cavity to produce a flat external surface (duct B). However, the duct leading edge separation angle and resultant effective blockage (blockage of duct and recirculation cell combined) are also reduced, and a corresponding reduction in peak power coefficient ensues. The reduced size recirculation region adjacent to the external surface of duct B is visible in Fig. 8. The effect of external surface curvature on basin efficiency and power extraction is illustrated in Fig. 9, where ducts B and C are compared.

While the power coefficient is of primary concern with regard to device performance, basin efficiency must also be considered. A high basin efficiency is desirable for devices operating in arrays, as more of the resource is conserved and available for further power extraction by other devices. While individual devices may not extract maximum power locally, the array as a whole acts to remove the maximum amount of power for a given drop in free-surface height (i.e. total power removal).

In an effort to achieve an improved balance of power coefficient and basin efficiency, a new design, duct H, is generated. Duct H is produced by combining the desirable features identified in the analysis of duct curvature presented above: the internal surface of duct D and the external surface

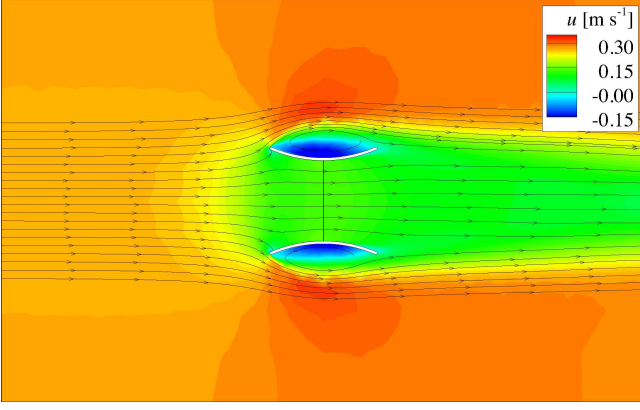


Fig. 7. Contours of streamwise velocity, u , on a horizontal midplane through the centre of device C, with instantaneous pathlines superimposed. A region of recirculating flow is visible adjacent to the external surface of the duct ($K_L = 4.0$, $C_T \approx 0.589$).

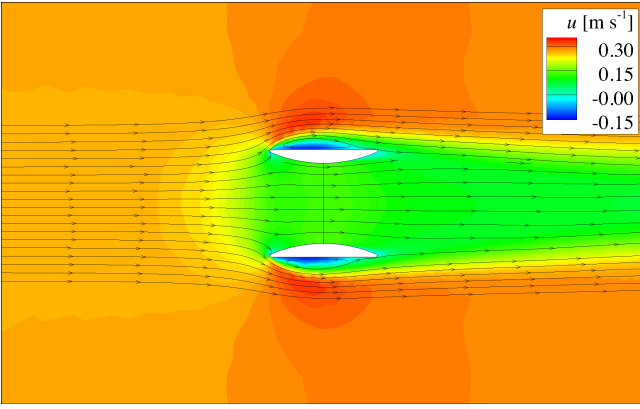


Fig. 8. Contours of streamwise velocity, u , on a horizontal midplane through the centre of device B, with instantaneous pathlines superimposed. The recirculating flow adjacent to the duct exterior is smaller than the corresponding feature in device C (Fig. 7) ($K_L = 4.0$, $C_T \approx 0.587$).

of duct B.

Duct H is now compared with ducts B, D, E and the unducted device in Fig. 10. For each device, the operating point closest to the top right-hand corner of the graph is optimal in terms of producing the most power, i.e. highest C_P , for the least power removed from the flow, i.e. highest η . It is clear that for any given C_P the unducted device has the highest basin efficiency η . The ducted devices generally have lower basin efficiencies due to the additional loss mechanisms associated with added streamwise loading, or drag, on the duct. A significant increase in basin efficiency may be achieved at the expense of a small reduction in power for all devices. Taking device H as an example, when the disk loading is reduced by 22.4%, the basin efficiency increases by 16.3%, while the power coefficient drops by only 3.2%.

Duct H is chosen for further simulation with higher-order rotor models. Note however that there is little discernible difference between duct H and a straight pipe (duct E).

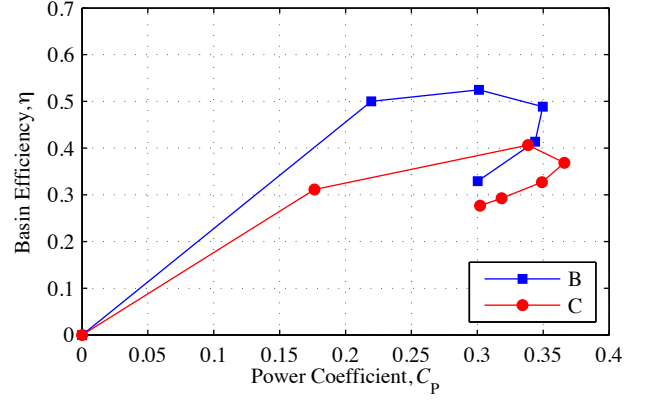


Fig. 9. Effect of external duct surface curvature on power coefficient and basin efficiency.

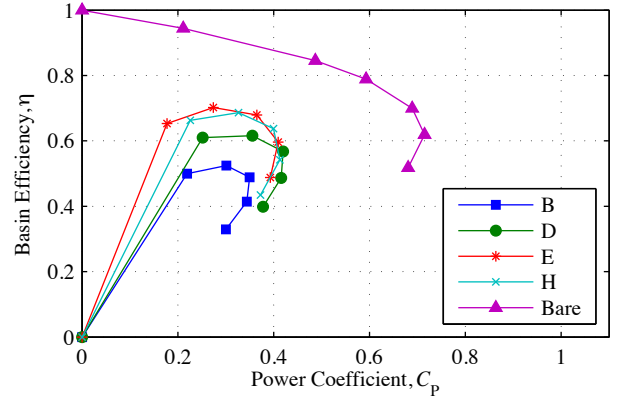


Fig. 10. Power coefficient and basin efficiency for bare (unducted) and a selection of ducted devices.

VI. ROTOR MODELLING

The focus of the preceding simulations was on duct performance, where it is acceptable to model the rotor as an actuator disk. Upper limits on device performance are given by the resulting power curves (see Fig. 3), however a real rotor will be unable to attain these limiting coefficient values due to effects of finite blade number and geometry as well as viscous effects and blade drag. We now seek to improved models of real ducted rotors through two methods of rotor modelling, which account for induced rotation in the flow and/or discrete blades. A better indication of overall device performance is expected. The simulations have been prepared to complement future experimental work. Duct H is to be constructed to match a 27 cm diameter three-bladed rotor, previously tested as an unducted device [12]. This rotor, which has a Goettingen 804 section with a 5% thick trailing edge, has been designed for unducted operation using a conventional BEM method [13].

The internal diameter of duct H in Fig. 1(h) is 35 cm, so that design is now geometrically scaled by a linear factor of $\frac{27}{35}$. The width and depth of the computational domain are as described earlier in Section III, resulting in a horizontal blockage of 20.6% (or a lateral inter-device spacing of $4.86D$),

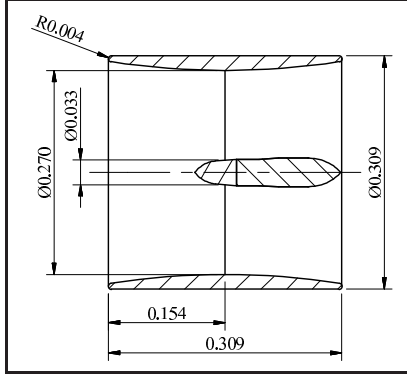


Fig. 11. Duct H scaled to fit a 27 cm diameter rotor. The hub geometry is based on a dynamometer originally designed to match the unducted rotor tested in [12]. All dimensions are in metres.

vertical blockage of 30.9%, and an area blockage of $b = 5\%$. A representative hub geometry, based on a dynamometer used in conjunction with the 27 cm diameter rotor in previous experiments [12], is also modelled (see Fig. 11).

The following sections describe the two rotor models employed; a RANS-embedded Blade Element Momentum Method and a Blade-resolved method in which the rotor geometry is fully meshed. This is followed by a comparison of the two rotor models with predictions from actuator disk modelling.

A. RANS-embedded Blade Element Momentum Method

In the RANS-embedded Blade Element Momentum method (henceforth referred to as RANS-BEM), the rotor is modelled in a disk region as a boundary condition [14], [15]. The rotor must be fully specified in terms of rotor geometry, blade section and tip-speed-ratio. Additionally, the blade lift and drag coefficients must be specified as a function of angle of attack. The rotor is not explicitly modelled but its presence is accounted for by imposing radially varying thrust and torque to the flow that are computed in response to the local flow-field. Numerically this is achieved by dividing the disk into a series of concentric annuli. Imposing the rotor loading on the annuli results in a radially varying set of discrete axial and circumferential induction factors (one per annulus). The solution proceeds by iteration until the flow-field, angle of attack and induction factors are in balance with the rotor loading model. The RANS-BEM method is a steady flow model which does not model the presence of discrete blades. Instead their presence is accounted for on a time-mean basis by considering blade loads to be uniformly and circumferentially distributed around each annulus. This technique enables arbitrary rotor blade geometries to be modelled without explicit resolution of the geometry. Instead, the blade section, twist and taper at each radial station are tabulated in a text file. For the present investigation, lift and drag data for the blade section (Goettingen 804, 5% trailing edge thickness) are calculated numerically for a representative Reynolds number of 20,000 and presented in Fig. 13.

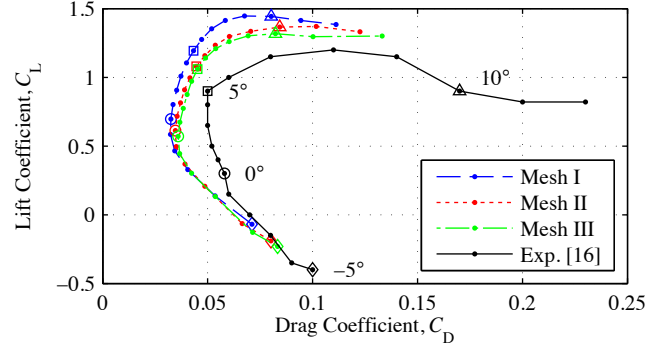


Fig. 12. Comparison of calculated and experimental [17] drag polars for three levels of mesh resolution. Angle of attack α is labelled in 5° increments ($Re = 30,000$; $-5^\circ < \alpha < 12^\circ$).

The RANS-BEM method features a tip-loss model which, when activated, accounts for losses associated with the generation of helical vortex structures from the tips of the rotor blades. Production of such structures is hampered by the duct, as shown in Fig. 17, so the tip-loss model is not employed for the present ducted rotor simulations.

A uniform inflow velocity of 0.27 m s^{-1} is specified at the inlet, which is located $5D$ upstream of the rotor plane. A uniform pressure of 0 Pa is set at the outlet, which is $5D$ downstream of the rotor plane. Symmetry boundary conditions are used on the floor, sidewalls and free-surface (rigid lid approximation). The effects of turbulence are modelled using the $k-\omega$ SST model as described in Section III.

Steady simulations are carried out over the full operating range (tip-speed-ratios $1 < \lambda < 7$) using the numerical aerofoil data presented in the following section. The tip-speed-ratio is defined as $\lambda = \omega(D/2)/u_\infty$, where ω is the angular velocity of the rotor.

B. Blade-Resolved Simulation

The second method of rotor modelling involves explicit meshing of the blade geometry, which leads to a large number of computational cells. This, together with the need for an unsteady solution, necessitates a large computational resource.

Accuracy of the “blade-resolved” method hinges on the correct prediction of blade forces, which is difficult to achieve at the range of Reynolds numbers in question (15,000 – 20,000) due to a number of flow mechanisms such as formation of laminar separation bubbles, the onset of transition, and highly three-dimensional anisotropic flows. A grid convergence study is carried out on a Goettingen 804 aerofoil section of unit chord and span to determine the degree of grid resolution required at the blade surface. Experimental data is available at Reynolds numbers of 20,000 [16] and 30,000 [17]. We choose to use the higher Reynolds number as this is expected to lead to more reliable experimental measured data due to increased force magnitude.

The forces on the blade are found to be most sensitive to boundary layer resolution, as opposed to general mesh density, so the meshes are refined on this basis. Surface elements have

TABLE I
DETAILS OF GRIDS USED IN BLADE CONVERGENCE STUDY.

Mesh	Node Count	Cell Count	Number of Layers of Prismatic Elements
I	66,938	222,753	8
II	74,331	230,850	10
III	82,049	229,555	12

a maximum in-surface dimension of $0.2c$ on the upper and lower surfaces, where c is the chord length. The maximum surface element dimensions at the leading and trailing edges are $0.0025c$ and $0.005c$ respectively. The boundary layer is resolved by a number of layers of high aspect ratio prismatic elements. The first cell height is set to $0.0007c$, achieving y^+ values of 1.0 or less at maximum lift-to-drag ratio (an angle of attack of 5°). Subsequent layers are increased in height using a growth factor of 1.2. Details of the three grids used in the convergence study are given in Table I, each having a different number of layers of prismatic elements. For purposes of robust mesh generation, the thin trailing edge modelled has a finite thickness of 0.5% chord.

A series of steady RANS simulations is carried out for each mesh for $Re = 30,000$, where the angle of attack, α , is varied from -5° to 12° . The lift and drag coefficients, C_L and C_D , for each operating point are recorded and plotted to produce the drag polar shown in Fig. 12, in which

$$C_L = \frac{F_L}{\frac{1}{2}\rho u_\infty^2 c} ; C_D = \frac{F_D}{\frac{1}{2}\rho u_\infty^2 c} \quad (12)$$

where F_L and F_D are the forces acting on the blade in the perpendicular and streamwise directions respectively. Whilst it is seen that the mesh converges acceptably, with the medium resolution mesh providing adequate grid resolution to achieve numerical convergence, there remain differences between the converged numerical solution and the experimental data. Of note however is that at the maximum lift-to-drag ratio ($\alpha = 5^\circ$) the computational model performs acceptably. The topology (near wall dimensions and growth rates) of the medium resolution mesh are used in all subsequent blade-resolved simulations.

The rotor will operate at a Reynolds number of 16,700 (at 80% span at tip-speed-ratio for peak power) and hence we present in Fig. 13 a comparison of numerically simulated and experimentally derived drag polars for $Re = 20,000$. While the Goettingen 804 section has a thin trailing edge, the rotor to be modelled has a trailing edge thickness of 5% chord. We therefore present in Fig. 13 two numerical polars for trailing edge thicknesses 0.5% and 5%, in order that the effects of thickness can be identified. As expected trailing edge thickness is seen to increase drag at all angles of attack. Comparison of the 0.5% thick numerical polar to the experimental data shows an under-prediction of drag. The errors are likely due to the difficulties in simulating such low Re blade flows as well as the inherent inaccuracies associated with low Re experiments.

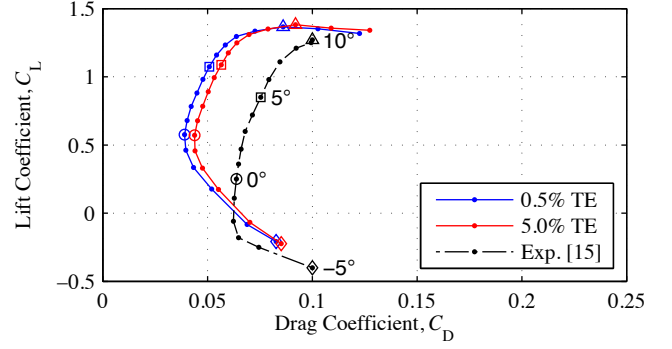


Fig. 13. Numerically computed drag polars for thin and thick trailing edge sections, compared with experimental data [16]. Angle of attack α is labelled in 5° increments ($Re = 20,000$; $-5^\circ < \alpha < 12^\circ$).

The RANS-BEM model utilises the numerical simulated 5% Trailing Edge thickness drag polar shown in Fig. 13.

The final mesh for the blade-resolved simulations is composed of 4.4 million cells. Based on the results of the blade convergence study, the boundary layers on the blade, duct and hub surfaces are resolved with ten layers of high aspect ratio prismatic elements, a first cell height giving a y^+ limit of 1.0 (for maximum lift-to-drag ratio) and a growth ratio of 1.2. For these simulations, the floor and sides of the flume are modelled as rough walls. A wall function is used to approximate the sheared velocity profile at these boundaries, which are resolved with a $y^+ \approx 100$. Four layers of prismatic elements with a growth factor of 1.2 are used to resolve the flume floor and wall boundary layers.

A uniform inflow velocity of 0.27 m s^{-1} , a turbulence intensity of 0.1% and a turbulent length scale of $D/2 = 0.1545 \text{ m}$ are specified at the inlet, located $5D$ upstream of the rotor plane. A uniform pressure of 0 Pa is set at the outflow, which is located $10D$ downstream. The effects of turbulence are modelled using the $k-\omega$ SST model as described in Section III.

Angular motion of the rotor is achieved through the use of a cylindrical rotating mesh region, which encompasses the rotor, hub and duct. The device is simulated in operation at tip-speed-ratios, λ , between 2.0 and 4.5 by specifying the corresponding angular velocity in the rotating domain. No-slip wall boundary conditions are applied at the rotor, hub and duct surfaces. The duct and hub are axi-symmetric, and although they rotate with the mesh, they are held stationary in the inertial frame by applying an angular velocity boundary condition of 0 rad s^{-1} in that frame. The floor and sides of the domain are treated as rough walls, with roughness parameters matching the walls of the experimental flume. Solution stability is aided by ramping both the inflow velocity and the rotor angular velocity from zero to the target value over the first half-revolution.

The timestep for each operating point is based on the chord length at 80% radius, and the angular velocity of the rotor. At the 80% radial station, the rotor blade travels 10% of the local chord length per time step. Once the inflow and rotor

TABLE II
ROTOR OPERATING POINTS SIMULATED BY RANS-BEM AND
BLADE-RESOLVED MODELS.

Tip-speed-ratio, λ	RANS-BEM	Blade-resolved
1.0	x	
2.0	x	x
2.5		x
3.0	x	x
3.5	x	x
4.0	x	x
4.5	x	x
5.0	x	
6.0	x	

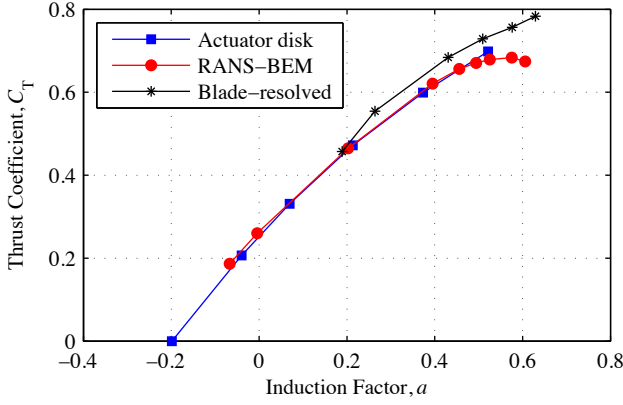


Fig. 14. A comparison of thrust performance predictions by actuator disk, RANS-BEM, and blade-resolved simulations.

velocities have ramped to their target values, each rotation is completed in approximately 375 timesteps.

VII. COMPARISON OF ROTOR MODELS

Results are now presented for three methods of rotor modelling. In each case, the rotor diameter is 27 cm and the external diameter of the duct is 35 cm (see Fig. 11). The upper limits on performance are predicted by the actuator disk rotor model; the hub is not modelled in this case. The RANS-BEM and blade-resolved models provide more realistic predictions of performance, as rotor geometry, hub geometry, and rotor motion are taken into account.

Some small differences exist between the rotor geometries used in the blade-resolved and RANS-BEM rotor models. These emanate from the use of exact and idealised rotor geometries; with the blade-resolved simulations exactly reproducing the rotor to be used in subsequent experiments, and the RANS-BEM rotor model being based on an idealisation of the experimental rotor. The main difference between the two is a thickening of the inboard sections of the real rotor to prevent failure during experiments. Further work will be carried out to match the geometries of the RANS-BEM and blade-resolved models and hence improve the agreement between the respective predictions of performance.

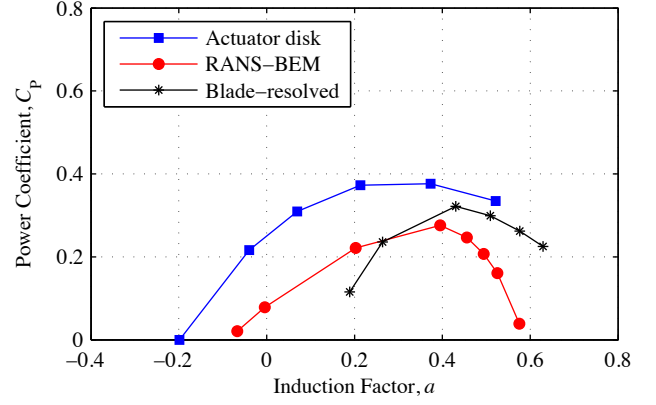


Fig. 15. A comparison of power performance predictions by actuator disk, RANS-BEM, and blade-resolved simulations.

The three models are compared in terms of power, thrust, and basin efficiency in Figs. 14 – 16 respectively. To allow for comparison between all models, the operating state of the rotor is described in terms of the axial induction factor a . The RANS-BEM and blade-resolved rotors are simulated at a range of tip-speed-ratios (see Table II), for which equivalent axial induction factors are subsequently calculated. As expected, the induction factor increases with tip-speed-ratio.

An effect of basing rotor performance comparisons on induction factor is that the thrust predictions for each model fall quite close together, as illustrated in Fig. 14.

Figure 15 shows that the RANS-BEM and blade-resolved models perform well relative to the actuator disk limit, with the reduction in power caused by viscous effects and rotor design. Note that the rotor was originally designed for unducted operation, and a rotor designed specifically for ducted operation would be expected to operate closer to the actuator disk limit. Overall device performance would still be significantly poorer than that of an unducted device, as indicated by the actuator disk limits shown in Fig. 3.

Generally, the basin efficiency of the RANS-BEM and blade-resolved models is lower than that of the actuator disk model; see Fig. 16. This is due to the extra losses introduced by viscous effects, blade drag, and wake rotation.

A qualitative difference is discernible between the basin efficiency characteristic predicted by the actuator disk model and that predicted by the higher-order rotor models. The actuator disk model indicates that a broad peak power region exists, along which the basin efficiency varies. For the other models however, a sharp operating point where power and efficiency are at their highest is predicted.

One pertinent feature of the flow field around the ducted turbine, as calculated (Fig. 17) is that a helical tip-vortex structure, readily identifiable in unducted rotor wakes, is not discernible. This is attributable to the bounding effect of the inner duct wall. Here, bound circulation is maintained to the blade tip, thus limiting the production of a tip vortex. The decision not to use a tip-loss model in the corresponding RANS-

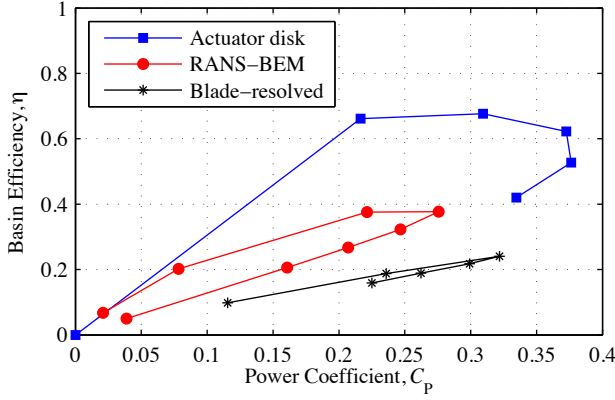


Fig. 16. A comparison of basin efficiency predictions by actuator disk, RANS-BEM, and blade-resolved simulations.

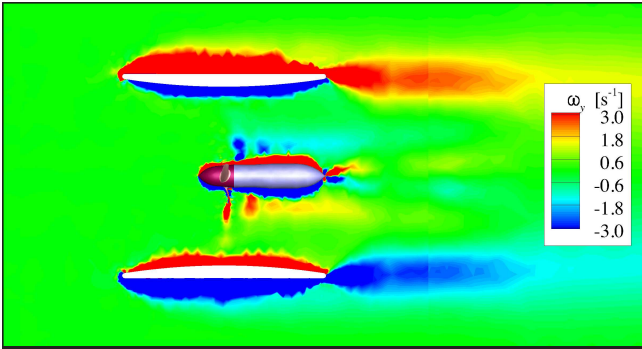


Fig. 17. Instantaneous contours of the vertical component of vorticity, ω_y , on a horizontal midplane through the ducted device. The intersection of the helical root vortices with the midplane is visible.

BEM simulations is hence justified. Vorticity responsible for flow retardation through the duct is shed from the trailing edge of the duct as a continuous sheet. Of note is that root vortices shed from the trailing edges of the rotor blades are visible.

The computational overhead associated with blade-resolved simulations of a ducted tidal turbine for a single operating point (around 2000 CPU-hours) is about two orders of magnitude greater than that associated with RANS-BEM simulations (around 8 CPU-hours). The computationally expedient RANS-BEM method is therefore well-placed for use in rotor design and device comparison.

VIII. CONCLUSION

The aim of this body of work has been to design a bi-directional duct for a ducted tidal turbine within given design constraints. The effects of internal and external duct surface curvature on device power coefficient and basin efficiency are identified through a series of comparative RANS simulations where the rotor is modelled as an actuator disk. An improved balance between power coefficient and basin efficiency is achieved by combining a flat external surface with a gently-curved internal surface to produce a new design. It is noted that, as performance is normalised on external device diameter,

the best bi-directional ducted device achieves a maximum power coefficient of only 57% of that of an unducted device.

More realistic indications of ducted device performance are given by higher-order rotor modelling techniques. As expected, both the RANS-BEM and blade-resolved models predict reduced power extraction and basin efficiency due to viscous losses and real rotor effects. Disparities between corresponding results of these two models are suspected to be due to differences in effective rotor geometry, and require further investigation.

The tip vortices usually associated with unducted rotor flows are not present for the ducted devices considered. Hence a tip-loss model is not appropriate for use in RANS-BEM simulations of ducted devices in which bound circulation is maintained to the duct wall.

Finally, the computational overhead of the RANS-BEM model is noted to be significantly smaller than that of the blade-resolved model.

ACKNOWLEDGEMENT

This work has been carried out as part of the PerAWaT project, commissioned by the Energy Technologies Institute.

REFERENCES

- [1] Clean Current Power Systems Inc. (2011). [Online]. Available: www.cleancurrent.com
- [2] OpenHydro Group Ltd. (2011). [Online]. Available: www.openhydro.com
- [3] M. O. L. Hansen, N. N. Sorensen, and R. G. J. Flay, "Effect of placing a diffuser around a wind turbine," *Wind Energy*, vol. 3, pp. 207–213, 2000.
- [4] H. Grassmann, F. Bet, G. Cabras, M. Ceshia, D. Cobai, and C. Del-Papa, "A partially static turbine - first experimental results," *Renewable Energy*, vol. 28, pp. 1779–1785, 2003.
- [5] ANSYS Inc., *ANSYS FLUENT 12.0 User's Guide*, 2009.
- [6] C. S. K. Belloni and R. H. J. Willden, "A computational study of a bi-directional ducted tidal turbine." 3rd International Conference on Ocean Energy, 2010.
- [7] ANSYS Inc., *ANSYS ICEM CFD Help Manual*, 2010.
- [8] C. A. Consul, R. H. J. Willden, and S. C. McIntosh, "An investigation of the influence of free surface effects on the hydrodynamic performance of marine cross-flow turbines." European Wave and Tidal Energy Conference, 2011.
- [9] C. S. K. Belloni and R. H. J. Willden, "Flow field and performance analysis of bidirectional and open-centre ducted tidal turbines." European Wave and Tidal Energy Conference, 2011.
- [10] M. Shives and C. Crawford, "Overall efficiency of ducted tidal current turbines," in *OCEANS 2010*, sept. 2010, pp. 1–6.
- [11] S. Draper, G. Houlby, M. Oldfield, and A. Borthwick, "Modelling tidal energy extraction in a depth-averaged coastal domain," *Renewable Power Generation, IET*, vol. 4, no. 6, pp. 545–554, 2010.
- [12] T. Stallard, R. Collings, T. Feng, and J. I. Whelan, "Interactions between tidal turbine wakes: Experimental study of a group of 3-bladed rotors." European Wave and Tidal Energy Conference, 2011.
- [13] E. A. Bossanyi, "GH Bladed – Theory Manual," Technical Report 282/BR/009, 2003.
- [14] S. C. McIntosh, C. F. Fleming, and R. H. J. Willden, "Optimal axial flow tidal turbine design." European Wave and Tidal Energy Conference, 2011.
- [15] M. Harrison, W. Batten, and A. Bahaj, "A blade element actuator disc approach applied to tidal stream turbines," in *OCEANS 2010*, pp. 1 – 8.
- [16] S. J. Miley, "A catalog of low Reynolds number airfoil data for wind turbine applications," Department of Aerospace Engineering, Texas A&M University, College Station Texas 77843, RFP-3387 UC-60, 1982.
- [17] U. Hassan, "A wind tunnel investigation of the wake structure within small wind turbine farms." Technical Report ETSU WN 5113, 1993.